JOURNAL OF GEOPHYSICAL RESEARCH, VOL. 105, NO. D10, PAGES 12,381–12,396, MAY 27, 2000

Local mean state changes due to gravity wave breaking modulated by the diurnal tide

Han-Li Liu, Maura E. Hagan, and Raymond G. Roble

High Altitude Observatory, National Center for Atmospheric Research, Boulder, Colorado

Abstract. During gravity wave breaking, heating rates are determined by wave advection, turbulent diffusion, and turbulence dissipative heating. A series of numerical experiments show that the total heating rates can be larg ($\sim \pm 10$ Kh^{-1}) and can cause large local temperature changes. The wave advection causes dynamical cooling in most of the wave breaking region, consistent with previous studies. Nonuniform vertical turbulent diffusion causes strong transient heating in the lower part of the wave breaking region and cooling above. The dissipative heating rate is relatively small compared with those due to the dynamical cooling and turbulent diffusion. In these numerical experiments, zonal wind and temperature perturbations of the diurnal tide and the zonal mean zonal wind and temperature compose the background state for the computation. This is used to examine the idea that temperature inversions, often observed in the mesosphere, are related to the gravity wave and tidal wave interactions. The simulation results show that the large temperature changes in this process can form temperature inversion layers that progress downward with a speed similar to that of a diurnal tide phase speed, which clearly suggests the tidal modulation of the gravity wave and mean flow interactions. Such a process is dependent on season and latitude, because the background state stability varies with season and latitude. The development of the temperature inversion is also affected by the gravity wave characteristics. It is also shown that the local mean wind, wind shear, and chemical species can undergo large changes accompanying the temperature inversion.

1. Introduction

Atmospheric internal gravity waves can interact with mean flow and change the mean wind, temperature, turbulent transport, and chemical species in a significant way when the gravity wave becomes unstable and breaks [e.g., *Fritts,* 1984; *Walterscheid and Schubert,* 1990; *Fritts et al.,* 1994; *Liu et al.,* 1999]. Specifically, the importance of the interaction with the mean wind and global momentum budget is well established. The changes in temperature and chemical species, however, are relatively less understood. To determine the changes in temperature, not only transport due to wave advection is important, but also quantitative knowledge of turbulent diffusion and dissipative heating. Furthermore, the wave advection itself is also closely related to turbulent diffusion [*Walterscheid,* 1981]. The details of such turbulent processes in the mesosphere, however, are not well understood.

On the other hand, numerous observations have shown that "temperature inversion" layers exist in the mesosphere [e.g., *Schmidlin,* 1976; *Hauchecorne et al.,* 1987; *Dao et al.,* 1995; *Meriwether et al.,* 1998; *Leblanc et al.,* 1999a, b]. These measurements show that the temperature at the inversion layers can be 20 – 30 K larger than the climatological mean values, with associated short-term heating rates of the order of 10 Kh^{-1}, much larger than theoretical predictions [*Tao and Gardner,* 1995; *Leblanc et al.,* 1999a, b]. It was also found that the inversions are often associated with an overlying nearly adiabatic lapse rate, indicating a well-mixed turbulent layer [*Whiteway et al.,* 1995]. Numerical experiments of gravity wave breaking due to monochromatic gravity wave source and realistic tropospheric wave sources also show the existence of temperature inversion layer at the wave breaking level due to turbulent mixing [*Liu et al.,* 1999; *Holton and Alexander,* 1999]. The observed inversion layers also indicate temperature perturbations with spatial and temporal characteristics similar to the tidal waves, but the amplitudes are much larger than those predicted by the global-scale wave model (GSWM) [*Dao et al.,* 1995; *Meriwether et al.,* 1998]. *Meriwether et al.* [1998] therefore proposed that the large temperature changes and the temperature inversion layers are due to the interactions between gravity wave and tidal wave. This idea was tested in the numerical study by *Liu and Hagan* [1998].

Paper number 1999JD901163.
0148-0227/00/1999JD901163$09.00

In this work we intend to further address issues that are closely related to the observations: the temperature changes during gravity wave breaking, the tidal modulation of such changes, and the formation and development of the temperature inversion layers. A two-dimensional numerical model is used for the investigation. From the results of the numerical experiments, heating and cooling due to wave advection, turbulent diffusion, and turbulence dissipative heating are analyzed to study the causes of the temperature changes. Diurnal tidal wind and temperature perturbations as well as zonal mean states are used as the background atmosphere so that the tidal modulation of the gravity wave and mean flow interaction can be studied. The implication of the seasonal and latitudinal variation of the background state on the gravity wave stability is studied in a series of numerical experiments. The sensitivity to characteristics of gravity wave sources is also studied. Dynamical and chemical changes associated with the temperature inversion are discussed in light of the numerical results.

By using the turbulence model in the simulation, it is possible to establish a link between the wave breaking and the temperature inversion by relating the large heating rate values to the turbulent eddy diffusion coefficient. Therefore temperature inversion observations along with simultaneous measurements of wind and tracer species could be beneficial to further understanding of turbulence processes during gravity wave breaking in the mesosphere and to improve turbulence parameterization.

2. Numerical Methods

The numerical model used in this study solves the two-dimensional, nonlinear Navier-Stokes equations in a nonrotational system. A turbulence model is used for its closure, and it is also coupled with a middle-atmosphere chemistry model [*Liu et al.*, 1999]. Zonal mean and diurnal tidal winds and temperatures from the GSWM [*Hagan et al.*, 1999] are imposed as the background state for the calculation,

$$\frac{\partial \rho}{\partial t} + \nabla \cdot ((\rho_T + \rho)(\mathbf{V_T} + \mathbf{v})) = 0, \quad (1)$$

$$\frac{\partial \mathbf{v}}{\partial t} + (\mathbf{V_T} + \mathbf{v}) \cdot \nabla(\mathbf{V_T} + \mathbf{v}) + \frac{1}{(\rho_T + \rho)} \nabla(p_T + p) + g\mathbf{k} = \nu \frac{\partial^2 \mathbf{v}}{\partial x^2} + \frac{\partial}{\partial z}((\nu + K_m)\frac{\partial}{\partial z}\mathbf{v}), \quad (2)$$

$$\frac{\partial \theta}{\partial t} + (\mathbf{V_T} + \mathbf{v}) \cdot \nabla(\theta_T + \theta) = \nu \frac{\partial^2 \theta}{\partial x^2} + \frac{\partial}{\partial z}((\nu + K_h)\frac{\partial}{\partial z}\theta) + Q\frac{\theta_T + \theta}{c_p(T_T + T)}, \quad (3)$$

where ρ, p, θ, T, and $\mathbf{v} = (u, w)$ are the gravity wave density, pressure, potential temperature, temperature, and velocity fields, respectively. $\mathbf{V_T} = (U_T(z,t), 0)$ is the zonal mean wind plus the horizontal component of the GSWM tidal wind profile; ρ_T, θ_T, and p_T are the zonal mean plus tidal components of density, potential temperature, and pressure, respectively; g is gravity acceleration, and $\mathbf{k} = (0, 1)$; Q is the diabatic heating, which is turbulence dissipative heating in our numerical experiments. The molecular viscosity coefficient ν is assumed to be equal to the molecular diffusion coefficient. The eddy viscosity and diffusion coefficients, K_m and K_h, respectively, are calculated from the 2.5 level second-moment closure turbulence model [*Mellor and Yamada*, 1982; *Yamada*, 1983]. This turbulence model considers the diffusive and advective transport of turbulence as well as its production and decay. Equations (1)-(3) and the assumptions are similar to those in the work of *Liu and Hagan* [1998], although the tidal temperature perturbation was not considered there. It is worth noting that we impose the tidal forcing in the form of the slowly varying background fields with tidal characteristics. This forcing will generate responses in the density, temperature, and velocity fields with spatial and temporal scales similar to that of the tidal wave. However, these responses are relatively small compared with the gravity wave perturbations in our experiments, and it is assumed that all changes calculated from the equations above are associated with gravity wave and wave breaking. The local mean state changes are determined by averaging the field variables over the horizontal computational domain at each altitude to remove wave transience.

GSWM is a two-dimensional, linearized, steady state numerical tidal and planetary wave model which extends from the ground to the thermosphere [*Hagan et al.*, 1993, 1995, 1999]. The most recent version of the model is known as GSWM-98 [*Hagan et al.*, 1999]. Aggregate GSWM-98 zonal mean fields and migrating diurnal tidal results are used to specify the background state for the calculations we report herein and are briefly discussed below.

The GSWM-98 zonal mean background temperatures and densities are specified by MSISE90 [*Hedin*, 1991]. Tropospheric and lower stratospheric ($z < 20$ km) zonal mean zonal winds are from the semiempirical model of *Groves* [1985, 1987] with 7-year monthly averaged UARS high-resolution Doppler imager (HRDI) climatologies aloft [*Hagan et al.*, 1999]. Figure 1 illustrates the GSWM-98 background temperature and zonal wind fields for January and April conditions between 50 and 125 km and equatorward of 60°. As described below, it is within this region of the atmosphere that the upward propagating diurnal tidal components maximize. It is also where gravity waves become sufficiently large that they break. Therefore it is reasonable to expect that gravity waves may be profoundly affected by the diurnal tide in this regime.

The GSWM-98 migrating diurnal tidal forcing and dissipation parameterizations are also specified a pri-

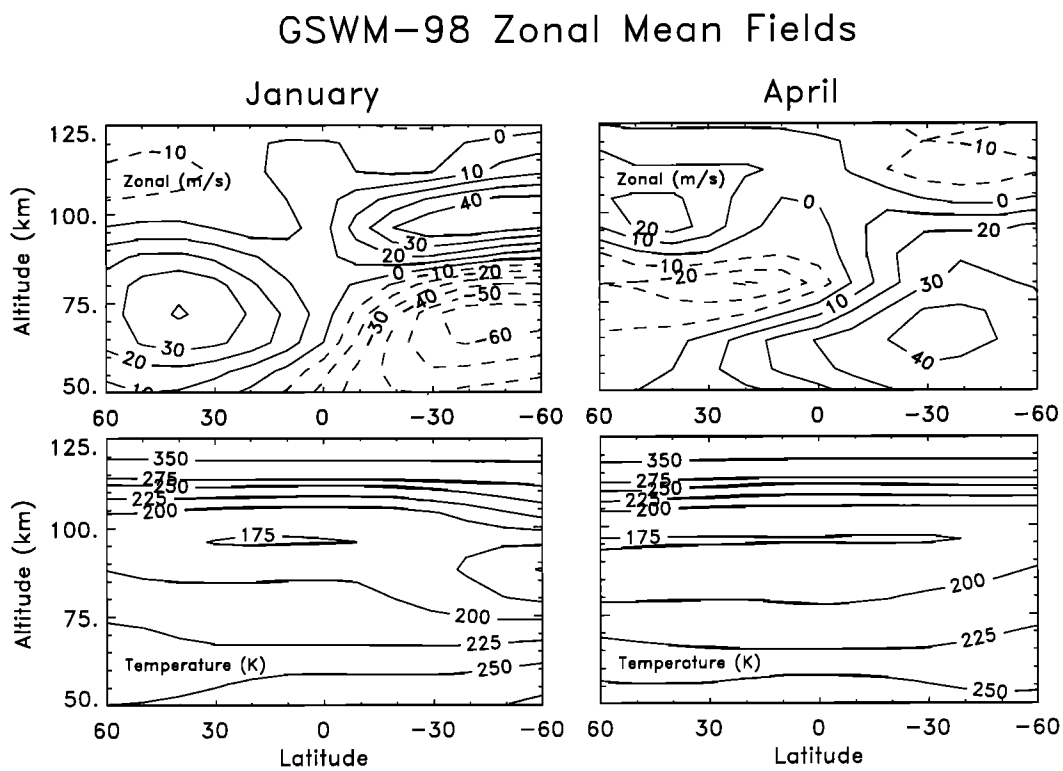

Figure 1. GSWM-98 background zonal wind (top figures) and temperature (bottom figures) fields for January (left column) and April (right column) conditions.

ori and are described in detail by *Hagan* [1996], *Hagan et al.* [1999], and references therein. In brief the migrating diurnal tide propagates westward with the apparent motion of the Sun and is primarily excited by the absorption of solar radiation throughout the atmosphere. Some components of the diurnal tide that are excited in the lower atmosphere grow in amplitude as they propagate upward and significantly affect the large-scale dynamics of the upper mesosphere and lower thermosphere (MLT) before they dissipate. Figure 2 illustrates the salient features of the GSWM-98 MLT migrating diurnal response. Diurnal amplitudes peak at $\sim$ 100 − 110 km. Temperature amplitudes maximize in the equatorial region, which is where the diurnal vertical velocity perturbations also peak (not illustrated). Both horizontal wind components are comparatively weak at the equator and in the tropics, however. Zonal wind amplitudes maximize near $\pm 30°$ (Figure 2), while meridional diurnal amplitudes peak some 10° equatorward of the zonal component. The GSWM-98 predicts a migrating diurnal tidal vertical wavelength of $\sim$ 30 km in the MLT (not illustrated). Figure 2 also illustrates the strong seasonal variations in GSWM-98 migrating diurnal temperature and zonal wind amplitudes. The tide is stronger in April (equinox) than it is in January (solstice). These and additional GSWM-98 results can be obtained at http://www.hao.ucar.edu/public/research/tiso/gswm/gswm.html.

The gravity wave stability is determined by the vertical gradient of the total potential temperature and the vertical wind shear due to the gravity wave, the zonal mean state, and the tidal perturbations. Because of the seasonal and latitudinal dependency of the zonal mean state and the tidal perturbations, tidal modulation of gravity wave stability is expected to show similar dependency. In this study, four numerical experiments are performed with the same gravity wave source but with zonal mean state and tidal perturbations at different seasons and latitudes, namely, January at 39°N (J39), April at 39°N (A39), January at the equator (JEQ), and April at the equator (AEQ). These locations were chosen because, as described above, the diurnal tidal temperature and zonal wind effects are most pronounced at equatorial and middle latitudes, respectively. In all these numerical experiments, the gravity wave source is always a westward monochromatic wave with a horizontal wavelength of 50 km and a period of 1600s (corresponding to a horizontal phase speed of 31.25 ms^{-1}), and the horizontal span of the computation is over one wavelength (50 km) in the zonal direction. These wave characteristics have been chosen to be consistent with observations [e.g. *Swenson et al.*, 1995] and such that the wave may not encounter a critical level before it breaks. The vertical velocity perturbation at the lower boundary (20 km) is 0.05 ms^{-1}, and the effective computational domain extends vertically to 120 km. Each run starts from local noon and stops

at 2200 LT. To study the dependency of the temperature changes on the gravity wave characteristics, four additional experiments have been done using the J39 mean state and tidal perturbations. In two of the experiments (hereinafter referred to as J39s1 and J39s2) the gravity wave periods are set to 2200s and 1100s, which correspond to horizontal phase speeds of 22.73 ms^{-1} and 45.45 ms^{-1}, respectively. In the other two experiments (J39s3 and J39s4) the wave period is still 1600s, but the amplitude of the wave varies with time after the start-up period, instead of remaining a constant. One of them (J39s3) has a single Gaussian shape amplitude peaking at 6400s with 3200s half width, while in the other one (J39s4), the source is a superposition of five Gaussian wave sources identical to the previous one with peaking time at 6400, 12800, 19200, 25600, and 32000s. In both experiments the peak wave amplitudes of the sources are the same as a constant amplitude of 0.05 ms^{-1}. These four additional experiments are used to study the spectral dependency of the results (J39s1 and J39s2) and the effects of single and multiple wave packets (J39s3 and J39s4). The analysis will focus on the results from the J39 case. Selected results from the other experiments will be presented for comparison.

3. Results and Analysis

In this section the heating rates associated with gravity wave breaking are analyzed. The corresponding temperature changes and the temporal evolution of such changes are discussed and related to tidal modulation. The implication of the seasonal and latitudinal variation of the tidal wave is explored by comparing the results from J39, A39, JEQ, and AEQ experiments. The sensitivity of the results to gravity wave source characteristics is studied by comparing experiments J39, J39s1, J39s2, J39s3, and J39s4. The dynamical and chemical effects associated with wave breaking are also examined.

3.1. Heating Rates Associated With Gravity Wave Breaking

In the mesosphere and mesopause region, heating rates related to dynamical processes are determined by the wave advection of heat (or equivalently, the divergence of the vertical wave heat flux), turbulent diffusion (eddy diffusion), and turbulence dissipative heating, as described by equation (3). Molecular diffusion is relatively insignificant in the mesosphere and mesopause region, about 1 m^2s^{-1} at 80 km and 8 m^2s^{-1} at 90 km [*Banks and Kockarts,* 1973], which is 1 to 2 orders of magnitude smaller than the average eddy diffusion coefficient at these altitudes. Figure 3 shows the local mean heating rates at 1600 LT (4 hours after initialization). The wave breaks at about 80 km at this time. From this figure it can be seen that the wave advection (dotted line) causes dynamical cooling in most of the breaking region. It peaks at about 85 km with a cooling rate of about -7 Kh^{-1}. In the lower part of the breaking region it causes heating, but the maximum value is

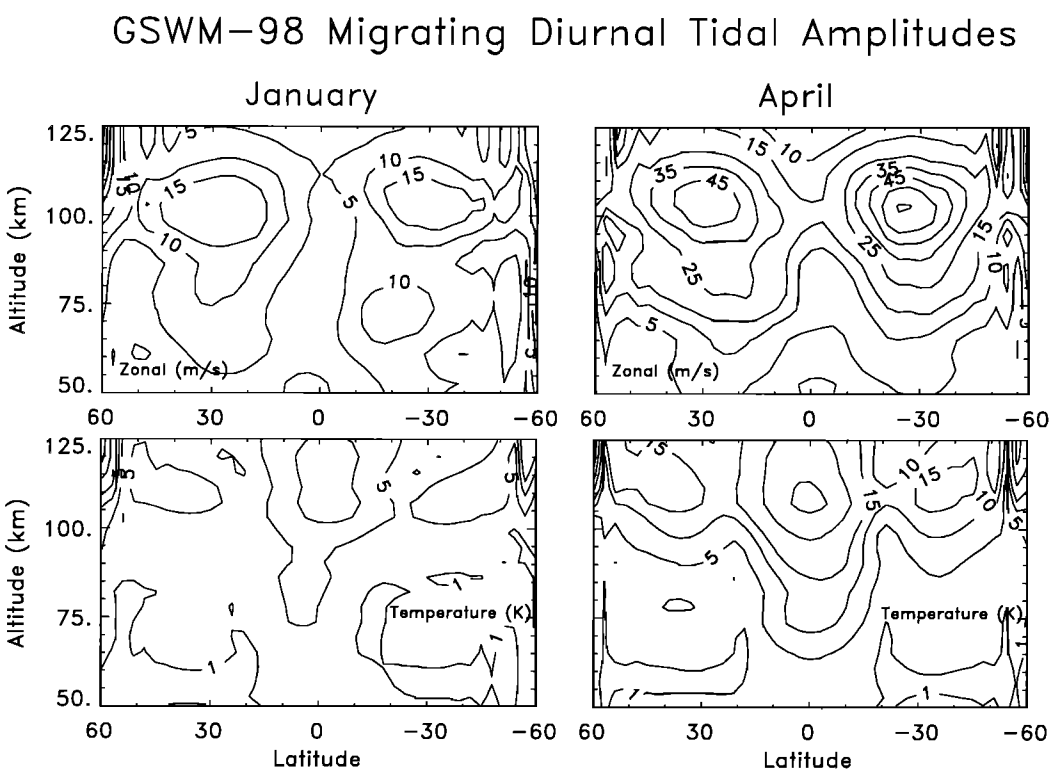

Figure 2. GSWM-98 migrating diurnal zonal wind(top row) and temperature (bottom row) amplitudes for January (left column) and April (right column) conditions.

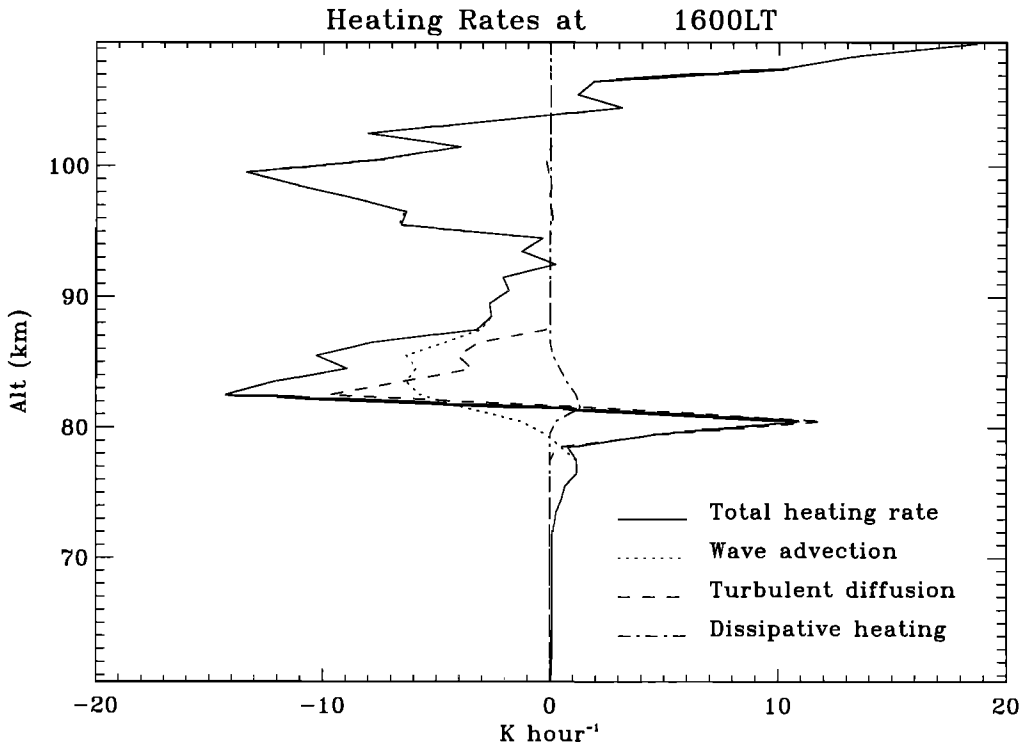

Figure 3. Local mean heating rates due to wave advection, turbulent diffusion, and dissipative heating in J39.

relatively small, 1 Kh^{-1} (77 km). The dynamical cooling in the breaking region is consistent with previous results, indicating that turbulent diffusion of the gravity wave potential temperature perturbation induces a downward wave heat flux and that the divergence of the downward wave heat flux may cause cooling [*Walterscheid,* 1981; *Gardner and Yang,* 1998]. On the other hand, at the early stage of the wave breaking, the localization of the turbulence may cause an upward heat flux and heating. It should be noted that the mean wave advection of heat is quite noisy because it is the sum of two relatively large terms with opposite signs (mean horizontal and vertical advection). Therefore in post-processing and plotting, the mean advection has been smoothed.

Figure 3 shows that the turbulent diffusion of the mean potential temperature causes large local heating and cooling over a narrow height range. In the upper part of the breaking region it causes cooling comparable with that by wave advection, -10 Kh^{-1} at 82.5 km; while at the lower part, it produces a heating rate of 11.5 Kh^{-1} at 80.5 km. This is caused by the relatively thin turbulence layer, which leads to large values of the vertical derivative of the eddy diffusion coefficient. To demonstrate such relation and to estimate the heating rate as a function of the turbulence layer thickness, the mean eddy diffusion coefficient is assumed to have a Gaussian profile in the vertical direction peaking at z_0 with half width h, $K_h(z) = K_{h\max} \exp(-(z-z_0)^2/h^2)$, then the corresponding heating rate is approximately

$$\frac{T}{\theta}\frac{1}{\rho}\frac{\partial}{\partial z}\rho K_h\frac{d\theta}{dz} = \frac{N^2TK_h}{g}\left(-\frac{(1-\kappa)}{H} - 2\frac{z-z_0}{h^2}\right), \quad (4)$$

where H is the atmosphere density scale height, and κ is the ratio between the gas constant and the specific heat at constant pressure. It has been assumed that the atmosphere is isothermal and the Brunt-Väisälä frequency N is a constant. For a thin turbulence layer where $h << H/(1-\kappa)$, the second term in the parentheses of equation (4) can become significant. It can be shown that the maximum heating rate occurs at approximately $z_0 - h/\sqrt{2}$, with an amplitude of $\frac{N^2TK_{h\max}}{gh}\exp(-1/2)\sqrt{2}$. The maximum cooling has approximately the same amplitude and occurs $h/\sqrt{2}$ above z_0. The local heating and cooling rates due to the nonuniform turbulent diffusion are inversely proportional to the square of the thickness of the turbulence layer, and proportional to the eddy diffusion coefficient. Letting $N = 0.02s^{-1}$, $T = 200$ K, and $h = 2.5$ km, it then requires that $K_h = 990m^2s^{-1}$ to produce a heating rate of 10 Kh^{-1}, which is consistent with the numerical results. On the other hand, although eddy diffusion produces large instantaneous heating and cooling rates, the parts due to $\partial K_h/\partial z$ may cancel each on a longer timescale because of the downward movement of the wave breaking region. Therefore the strong heating and the temperature increase are highly transient.

The turbulence dissipative heating rate is assumed to be equal to the turbulence production rate, which is calculated by

$$P_{\text{turb}} \approx -\overline{< u''w'' > \frac{\partial u}{\partial z}} + \beta g \overline{< w''\theta'' >}, \qquad (5)$$

where the double prime designates turbulent perturbation, angular brackets for ensemble average, and the overbar for average over one horizontal wavelength; $< u''w'' >$ and $< w''\theta'' >$ are Reynolds stress and turbulent heat flux, respectively, and β is the coefficient of thermal expansion. The first term on the right-hand side is the shear production of turbulence, and the second term is the buoyancy production. The buoyancy production term may be important locally where the Richardson number $Ri < -1$ during the initial wave overturning. However, the shear production becomes more significant when Ri approaches 0 or becomes positive. The heating rate due to turbulence dissipation shown in Figure 3 is calculated by letting $< u''w'' >= -K_m \partial u/\partial z$, while ignoring the buoyancy production. The maximum is at about 81.5 km with a heating rate of about 1.2 Kh^{-1}.

The net effect including the heating/cooling due to wave advection, turbulent diffusion, and turbulence dissipative heating is a maximum heating rate of 11 Kh^{-1} at 80.5 km and a maximum cooling rate of 14 Kh^{-1} at 82.5 km. The wave advection causes strong cooling at the upper part of the breaking region. Eddy diffusion produces strong transient heating in the leading edge of the wave breaking region and cooling in the trailing edge. The turbulence dissipative heating is relatively small.

3.2. Tidal Modulation of Gravity Wave Breaking and Seasonal/Latitudinal Dependency

The gravity wave breaking level is affected by the stability of the background atmosphere, which in part depends on the zonal mean and diurnal tidal wind and temperature. Therefore the local heating and cooling associated with gravity wave breaking should also be modulated by the zonal mean and the tide. Figure 4 shows the total local mean heating rate as a function of local time and altitude. After the initial wave breaking at about 1400 LT at 110 km and shortly thereafter at 95 km, the breaking regions and the associated maximum heating/cooling descend with time. The descending rate of the wave breaking region is about 2.5–4.0 ms^{-1} during the first two hours and then decreases to about 0.37 ms^{-1} afterward. The former is close to the local vertical phase speed of the gravity wave, and the latter is approximately equal to the vertical phase speed of the diurnal tide in the mesosphere. This is an indication that the wave stability is the controlling mechanism at the beginning of wave breaking, but tidal modulation of the wave stability becomes more important during the latter stage of the development.

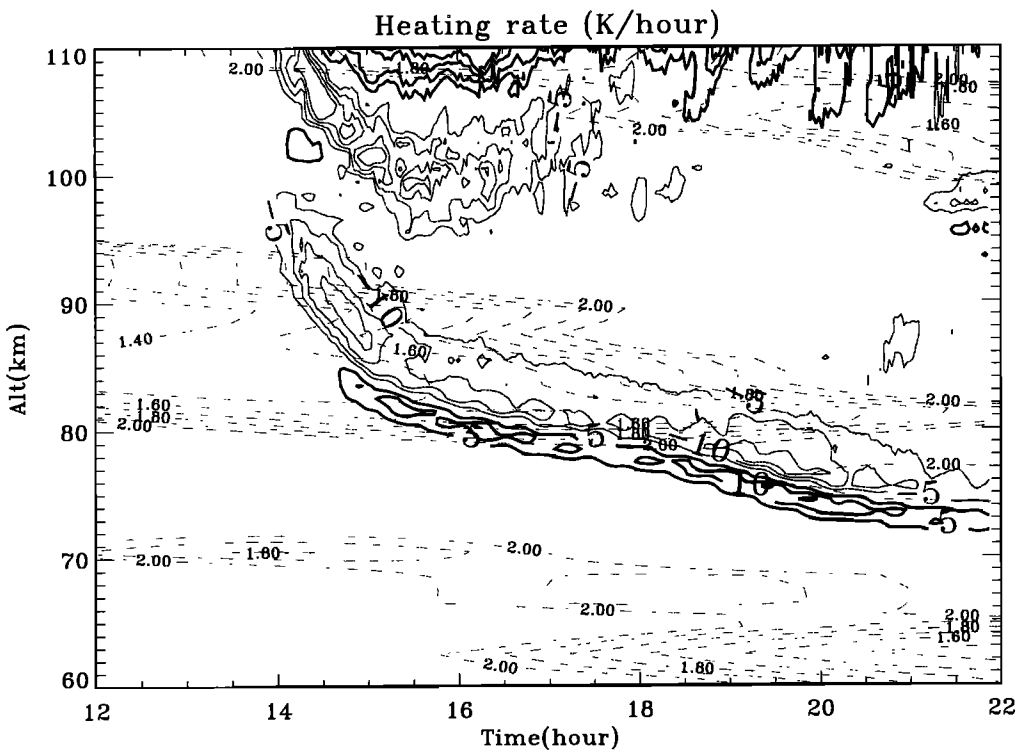

Figure 4. Local mean heating rate as a function of time and altitude. The thick solid contour lines are for net heating, and the thin solid curves are for net cooling. The dashed curves are the background state Richardson number on $\log_{10}$ scale.

Figure 4 also shows that the heating/cooling of the lower breaking region continues till the end of the simulation, but it only lasts for about 2 hours at higher altitudes. This is because that both breaking regions are generated by the same wave source, and when the breaking region at the lower altitudes fully develops, most wave energy is blocked there. The large heating rates above 105 km are mostly due to the advective heating from small-scale residue waves and low atmospheric density.

The tidal modulation can be examined quantitatively by looking at the Richardson number of the diurnal tide and zonal mean field Ri_0. For easy comparison this Richardson number contour is overplotted in Figure 4 (dashed lines) on a logarithm scale as a function of time and altitude. It clearly shows the downward phase progression due to the diurnal tide. Only contour lines with $Ri_0 \leq 200$ are shown, and the minimum is about 20. Although the background atmosphere is stable because $Ri_0 >> 1/4$, the tide does precondition the atmosphere so that the stability is nonuniform. Depending on the local time and altitude, there are regions where a gravity wave is more likely to become unstable than others. It can be seen from Figure 4 that the initial breaking occurs around the local minima of Ri_0. Furthermore, the development of the lower breaking region agrees well with the development of the local minima of Ri_0. As a result, the downward progression of the gravity wave breaking regions and the associated heating/cooling has similar temporal and spatial characteristics to those of the diurnal tide. It can also be seen that at each altitude the large heating and cooling rates (± 10 Kh^{-1}) would cancel each other on a timescale of a couple of hours and are therefore transient.

The strong transient heating and cooling are reflected in the temperature changes. Figure 5 shows the temperature profiles from 1230 to 2200 LT with half-hour intervals, and each profile is shifted to the right by 10 K. It should be noted that the temperatures are local mean values, which are obtained by averaging over one horizontal wavelength. Temperature perturbation due to diurnal tide is also included, whose amplitude and phase can be inferred from the the profiles before wave breaking in Figure 5. The strong transient heating produces a temperature inversion that can be as large as 17 K over the mean profile. Similar to the heating, the temperature inversion progresses downward along with the diurnal tide. Accompanying the temperature inversion, there is a large temperature decrease above corresponding to the strong cooling. The temperature decrease in the lower wave breaking region can be as large as -19 K, and the decrease in the higher one can be -50 K.

Because both diurnal tidal perturbations and the zonal mean states are seasonally and latitudinally dependent, it is reasonable to expect that the background

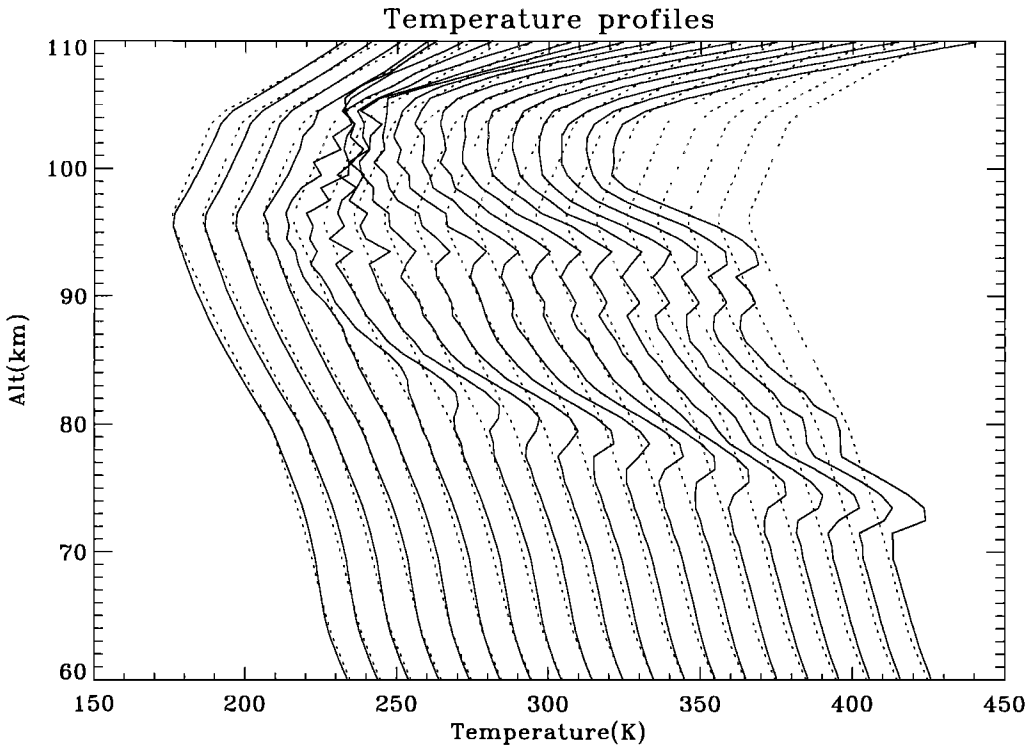

Figure 5. Temperature profiles from 1230 to 2200 LT with half-hour time intervals for J39. Each profile is shifted to the right by 10 K. The solid curves are profiles including zonal mean temperature, tidal perturbation, and local mean changes due to gravity wave breaking. The dotted curves are the zonal mean temperature profiles.

atmosphere stability and the modulation of the gravity wave breaking are also dependent on season and latitude. Figure 6 shows the Richardson number Ri_0 contours for J39, A39, JEQ, and AEQ based on the total zonal wind. It can be seen that they are very different. Ri_0 in J39 is relatively uniform distributed between 50 and 110 km during the 24-hour period, with a gap between 70 and 80 km. This is because the zonal mean zonal wind shear below 70 km and above 80 km is large at 39°N, and the zonal wind perturbation of the diurnal tide becomes large at higher altitudes (Figures 1 and 2). For JEQ, both the zonal mean zonal wind shear and the tidal perturbation are small, and the atmosphere is relatively stable. For A39 the zonal wind shear and the tidal wind perturbation are both important at higher altitudes; and for AEQ the wind shear at lower altitudes and very large tidal temperature perturbation at higher altitudes are the determining factors of the background atmosphere stability.

Because of the significant differences between the background atmosphere stability, the gravity wave stability and the associated temperature change are also different. Figure 7 shows the temperature profile changes from the four numerical experiments J39, A39, JEQ, and AEQ. It should be emphasized that the gravity wave sources are the same in all of these experiments. For JEQ the tidal temperature perturbation is the only temperature variation for most of the time of the simulation. The gravity wave begins to become unstable much later and causes some cooling in the breaking region around the mesopause. For A39 the most significant temperature increase is above the mesopause and this increase produces a local "double mesopause." The wave breaking location is consistent with the minimum background Richardson number. AEQ produces the most significant temperature increase below the mesopause. Excluding the tidal temperature perturbation of about 20 K, the increase is about 100 K. Because the gravity wave source specification may be artificial, the simulation results may not be realistic. However, these results do show the very significant seasonal and latitudinal dependency of the tidal modulation of gravity wave breaking for a uniform source.

The temperature inversions and their evolution shown in Figure 5 are similar to the lidar observations at Table Mountain (34.4°N) during winter (January and February) reported by *Leblanc et al.* [1999a]. The maximum amplitudes of the observed inversions (temperature value over monthly mean) are about $10-20$ K and large negative temperature perturbations are observed aloft (around 80 km). For example, the temperature profile at about 2000 LT on January 11, 1997 (third profile from the left in the third plot to the left-hand panel of Figure 1 in the paper) shows a temperature inversion between 66 and 70 km (maximum 15 K) and another one between 73 and 77 km (maximum 11 K). The latter one is similar to the simulation result which shows an inversion between 72 and 75 km (maximum 13 K) at 2000 LT. The inversions between 60 and 70 km were not reproduced in the simulation, probably because the specified gravity wave source is not large enough. On the other hand, the observed inversions between 60 and 70 km and their evolution during 1900–0500 LT closely follow the minimum Richardson numbers as shown in Figure 6 (January, 39°N), consistent with the above analysis.

The temperature measurements at Mauna Loa in October [*Leblanc et al.*, 1999b] shows that the temperature inversions are at higher altitudes ($80-90$ km), and the temperature structures are somewhat similar to those in simulations A39 and AEQ, where the minimum Richardson number region and wave breaking are at higher altitudes, as shown in Figures 6 and 7. However, direct comparison is not legitimate here because latitudes and seasons are not the same and semidiurnal tides, which become more significant at higher altitudes, are not included in the model. These measurements do show the strong latitudinal and seasonal dependency of the temperature inversion layers.

3.3. Sensitivity to Gravity Wave Sources

The complexity of the temperature structures in the these observations (especially during the winter) points to the complex nature of the gravity wave sources, which are usually transient, sporadic, and have a broad spectrum. On the other hand, other observations and numerical simulations have shown that one wave component may be dominant at a specific time and altitude due to wave dispersion, so that the wave appears quasi-monochromatic at that altitude [e.g., *Swenson et al.*, 1995; *Prusa et al.*, 1996]. Therefore a monochromatic wave source is still a good approximation. As mentioned in section 2, four additional numerical experiments with monochromatic or quasi-monochromatic wave sources have been conducted to study the sensitivity of the temperature changes to wave sources. The results are discussed in this section.

Figures 8a and 8b show the temperature changes in J39s1 and J39s2. Because the horizontal phase speed is smaller in J39s1 than in J39, the vertical phase speed and group velocity in J39s1 are also smaller, and the initial breaking is at a later time. After the initial breaking, the qualitative features of the temperature changes and the development of the temperature inversion layers between 70 and 80 km closely resemble those shown in Figure 5. Closer analysis shows that the amplitudes of these inversion layers are smaller (by less than 4 K), and their descending speed is slightly smaller than in J39. The smaller descending speed is due to the smaller vertical phase speed of the gravity wave in J39s1. Figure 8b shows that the initial wave breaking in J39s2 is earlier than in J39 and J39s1 because the vertical phase speed

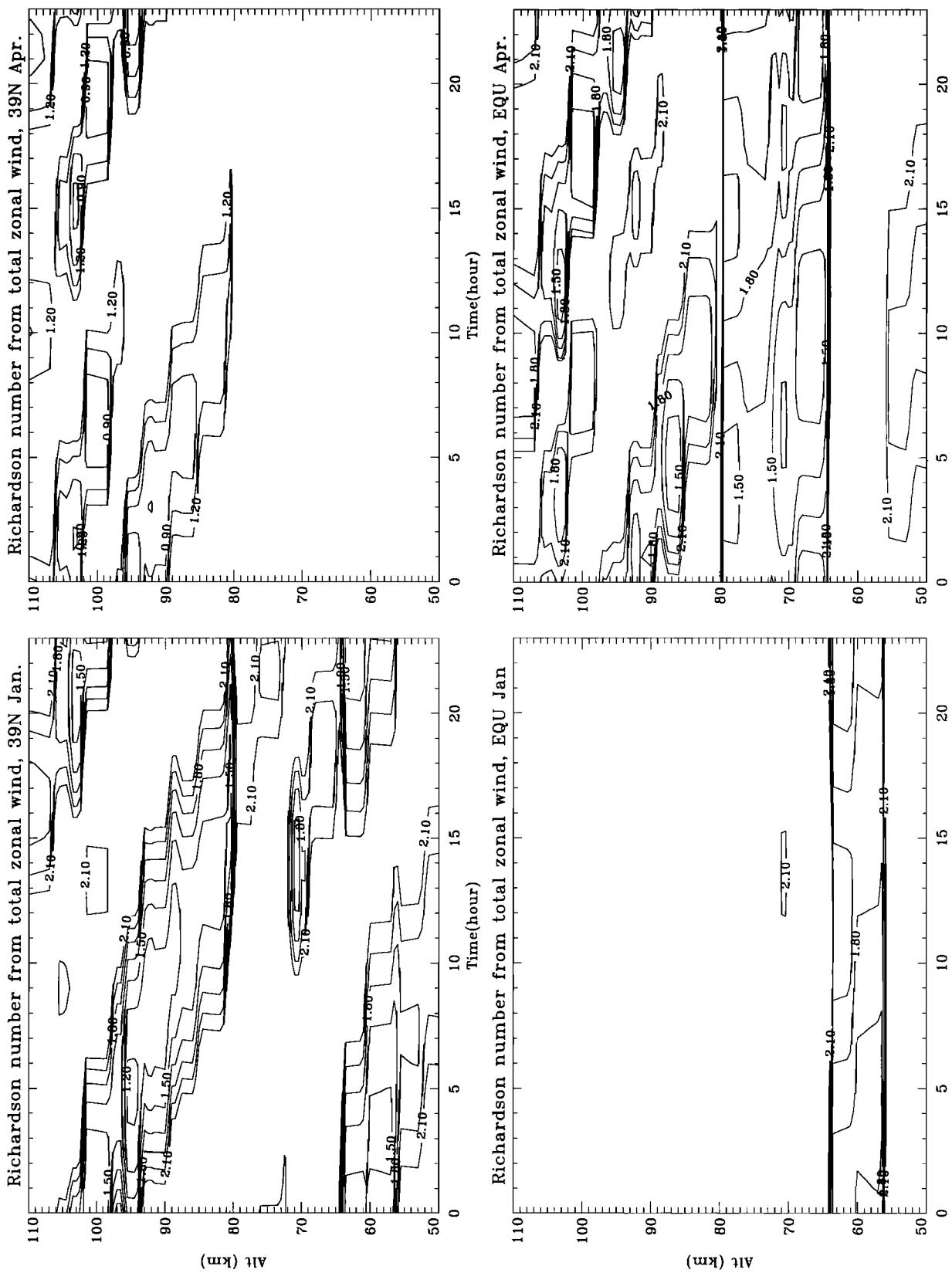

Figure 6. Contour lines of the background atmosphere (zonal mean and diurnal tide) Richardson number on $\log_{10}$ scale at 39°N (top row) and the equator (bottom row) and January (left column) and April (right column) over 24 hours.

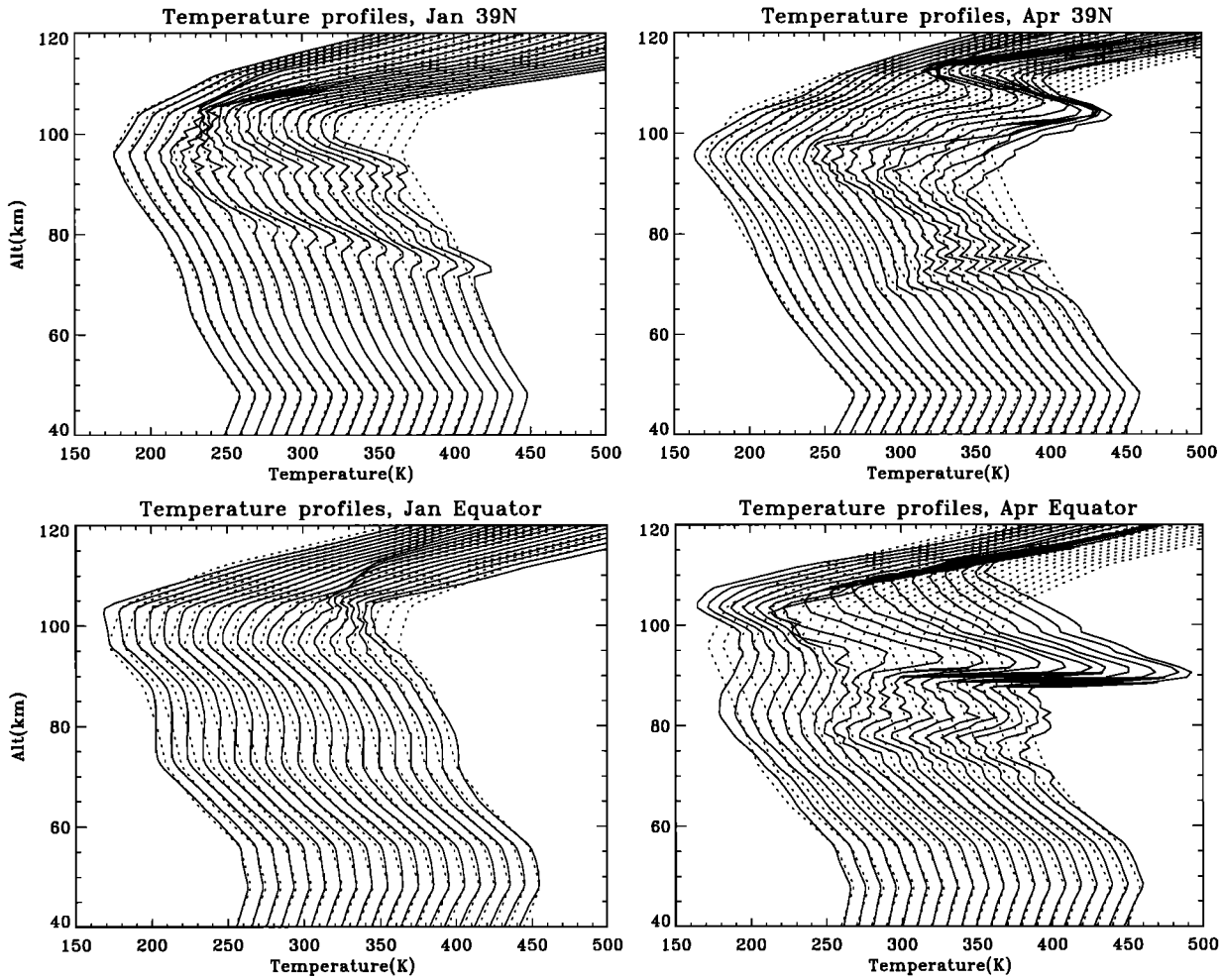

Figure 7. Temperature profiles for J39 (top left), A39(top right), JEQ(bottom left), and AEQ (bottom right) cases. Plotted in the same manner as Figure 5.

of the wave in J39s2 is larger. The development of the temperature inversions around 80 km in J39s2 is similar to that in J39 before 1800 LT, though the descending speed is slightly larger in J39s2. Again, this is due to its larger vertical phase speed. After 1800 LT, however, the descent of the inversion layers suddenly slows. This sudden change is because below about 76 km the specified gravity wave is stable and will not break with the tidal modulation. The breaking level can only extend to lower altitudes due to large wind shear created by wave-mean flow interactions [*Liu et al.*, 1999], and the rate is much smaller than the downward phase speed of the diurnal tide. Hereinafter this altitude is referred to as the "lowest breaking altitude." In J39 and J39s1 the waves have the same wave amplitude as in J39s2, but their vertical wavelengths are smaller. Therefore the maximum values of the potential temperature perturbation gradient at each altitude are larger in those two cases and their lowest breaking altitudes under the same background conditions are lower. The inversion layers have not reached down to these altitudes during the simulations J39 or J39s1.

Figures 9a and 9b are the temperature profiles for J39s3 and J39s4. In J39s3, a temperature inversion layer forms at about 83-85 km and moves downward during the early stages of breaking. As the peak of the wave passes and wave amplitude decreases, the wave becomes stable and the turbulence decays. Therefore the temperature inversion that forms during the wave breaking remains at the same amplitude and altitude, though the amplitude should decrease, if realistic radiative damping is considered. On the other hand, temperature changes due to multiple wave packets and breaking shown in Figure 9b are qualitatively very similar to those due to the persistent wave source in J39, with only small quantitative differences.

The results of these four experiments show that the tidal modulation of the wave breaking is significant above the lowest wave breaking altitude, and the corresponding temperature inversions show clear signatures of diurnal tide. At the same time, the exact location of wave breaking in the minimum Richardson number region and the descent speed of the wave breaking level are also affected by the wave characteristics. The low-

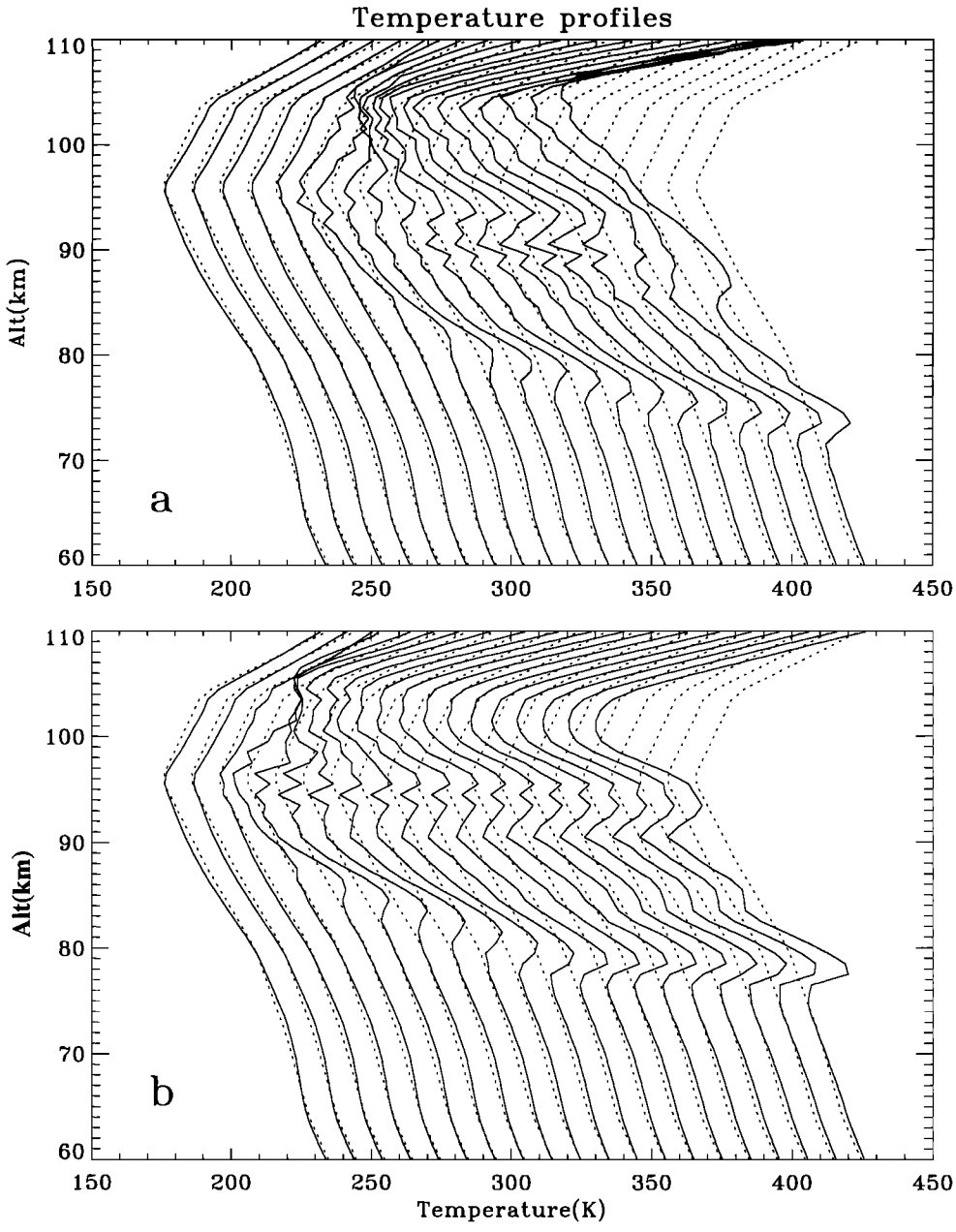

Figure 8. Temperature profiles for (a) J39s1 (phase speed smaller than J39) and (b) J39s2 (phase speed larger than J39). Plotted in the same manner as Figure 5.

est wave breaking altitude is determined by the wave amplitude and the vertical wavelength, as well as the background stability. When the wave breaking level and the corresponding temperature inversion reach this altitude, the speed of descent becomes much smaller than the vertical phase speed of the diurnal tide. Therefore changes in wave characteristics causes variations in the descent speed of the temperature inversions. This may provide an explanation for the differences in inversion layer descent speed in observations [*Leblanc et al.*, 1999a]. Such dependencies may be exploited further to deduce gravity wave characteristics from the observation of temperature inversions.

3.4. Related Dynamical and Chemical Effects

Gravity wave breaking causes mean flow acceleration which is also modulated by diurnal tide. Figure 10 shows the acceleration rate as a function of time and altitude. It can be seen that the acceleration due to wave momentum flux divergence is dominant. The westward acceleration peaks shortly after wave breaking with a maximum value of about 90 $ms^{-1}h^{-1}$. The acceleration associated with the wave breaking at higher altitudes decreases to virtually zero after 2 hours due to the blocking of wave energy by the wave breaking at lower altitudes. The wave breaking at the lower altitudes, on

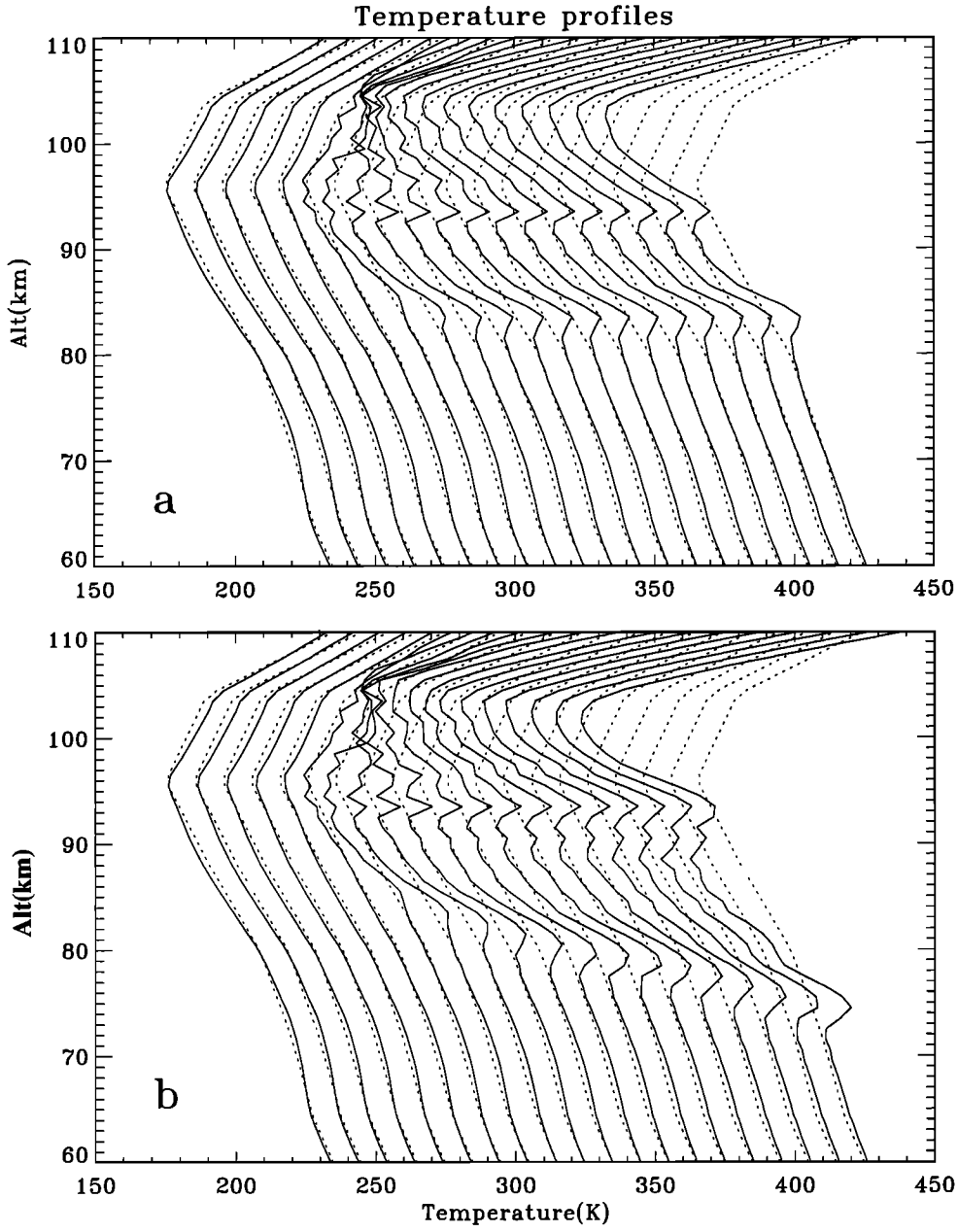

Figure 9. Temperature profiles for (a) J39s3 (single wave packet) and (b) J39s4 (multiple wave packets). Plotted in the same manner as Figure 5.

the other hand, further develops and progresses downward. By looking at the background Richardson number overplotted in this figure, it can be seen that such development is indeed modulated by the tidal wave influences on the atmospheric stability. The westward acceleration also increases the westward shear at the leading edge of the wave breaking region. Therefore there is a local mean wind acceleration and increase of wind shear accompanying the temperature inversion.

Figure 11 shows the vertical fluxes of atomic oxygen number density due to wave advection (solid line) and turbulent mixing (dotted line) at 1600 LT. Both fluxes are downward due to the increasing atomic oxygen mixing ratio with altitudes in the region. The downward flux due to wave advection peaks at 99 km, slightly higher than the peak altitude of the atomic oxygen number density (95-97 km). Therefore the number density of atomic oxygen increases at most altitudes below 99 km and decreases above, with the distinguished exception of the region between 82 km and 88 km. This is due to the strong nonuniform turbulent flux of atomic oxygen peaking at 82 km. In keeping with the the discussion in section 3.1 this nonuniform turbulent flux is related to the gravity wave breaking region. Therefore the number density of atomic oxygen tends to increase at the leading edge of the wave breaking level (along

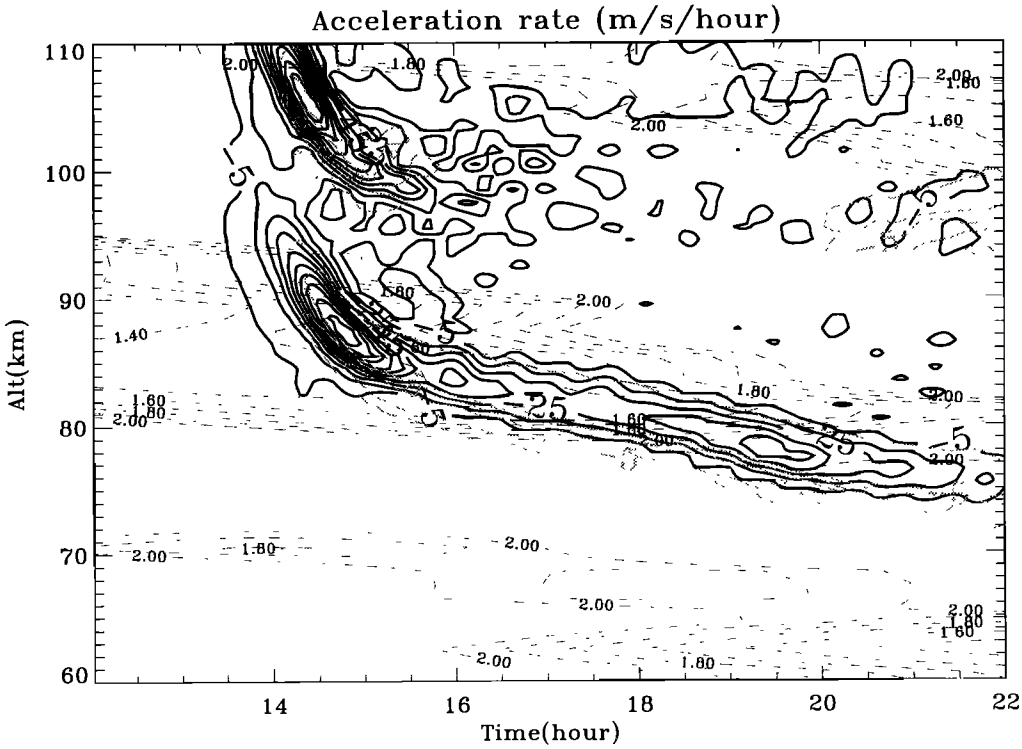

Figure 10. Acceleration rate as a function of time and altitude. The thick solid curves are for acceleration due to wave momentum flux divergence and the thin solid curves due to turbulent mixing. The negative values are for westward acceleration. The thin dashed curves are the background state Richardson number on $\log_{10}$ scale.

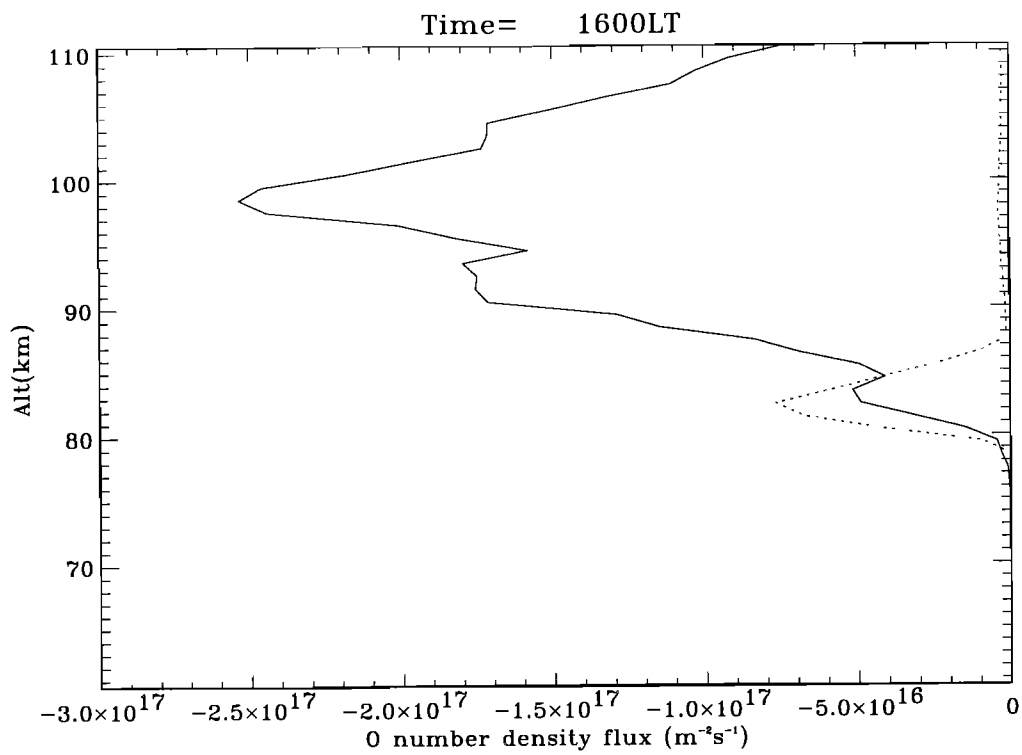

Figure 11. Number density fluxes of atomic oxygen due to wave advection (solid curve) and turbulent mixing (dotted curve).

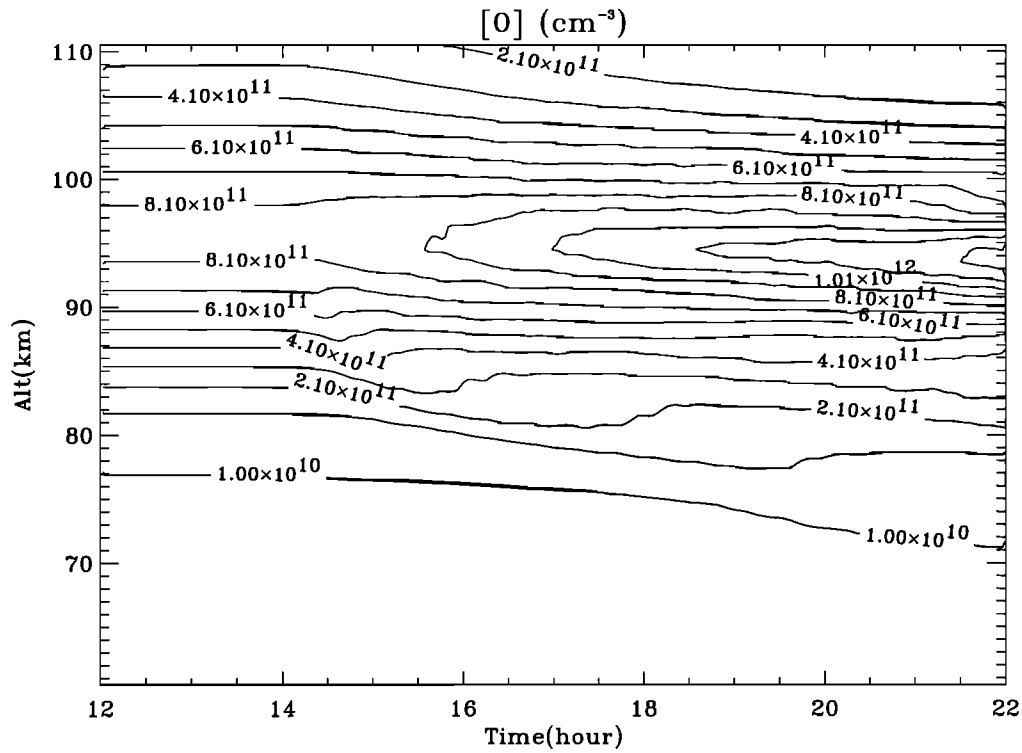

Figure 12. Atomic oxygen number density as a function of time and altitude.

with temperature increase) and decrease at the trailing edge. This tendency can be seen in Figure 12, which shows the local mean number density of atomic oxygen as a function of time and altitude. Accompanying the wave breaking region, the [O] changes in the 75–90 km altitude range are transient like the temperature changes in the same region. Because of the long chemical lifetime of atomic oxygen, the change in its number density is determined by the vertical transport due to both wave and turbulence. For chemical species with shorter chemical lifetimes such as ozone and OH, the process will be more complicated due to the coupling of the dynamics and the chemical processes [*Walterscheid and Schubert,* 1989].

4. Conclusions

The numerical experiments reported herein show that gravity wave breaking can cause significant local temperature changes. The variation of the vertical wave heat flux (wave advection) induces dynamical cooling in most of the wave breaking region. The turbulent eddy diffusion causes large transient heating and cooling ($\sim \pm 10$ Kh^{-1} in these experiments) at the leading and trailing edges of the descending breaking region, respectively. The turbulence dissipative heating rate is relatively small. The total heating and cooling due to thermal advection, eddy diffusion, and dissipative heating lead to large temperature decreases at the upper part of the wave breaking region and increases below. These changes form a structure commonly associated with a temperature inversion. The temperature inversion progresses downward over time along with the wave breaking region.

By analyzing the Richardson number of the background atmosphere, which includes the zonal means and the diurnal zonal wind and temperature perturbations from GSWM, we conclude that gravity wave stability is profoundly modulated by the tidal wave. The time and location of the initial breaking are affected by the background atmospheric stability. Further, the evolution of the breaking region has a clear signature of the diurnal tide. Therefore the temperature inversion associated with the wave breaking level can have a downward progression speed similar to the vertical phase speed of the diurnal tide. The experiments also show that such modulation has a strong seasonal and latitudinal dependence, because the diurnal tide and the zonal mean state vary with season and latitude.

The gravity wave characteristics (amplitude and vertical wavelength), along with the background state and tidal perturbations, determine the altitude below which the wave is stable. Above this altitude the temperature inversions from wave breaking are strongly modulated by the diurnal tide and are also affected by the gravity wave characteristics. The descent speed of the temperature inversions decreases significantly at this altitude.

The local mean wind, wind shear, and chemical species distribution all undergo significant changes at the temperature inversion layer in the numerical experiments.

Gravity wave breaking deposits momentum into the mean flow and causes mean flow acceleration. The enhanced vertical transport due to wave advection and turbulence mixing, as well as the temperature changes, affects the local chemical species. These can be used as diagnostic parameters for studying the temperature inversion. Furthermore, if the proposed mechanism is the cause of the temperature inversion layer, then the measurement of temperature inversion layers and the simultaneous measurements of wind and tracer species may yield very important information about gravity waves and turbulence in the mesosphere (e.g., the intrinsic phase speed of the dominant gravity wave mode and its amplitude, eddy diffusion coefficients, and Prandtl numbers).

In this study, only the modulation due to diurnal tide is considered, because observations [e.g., *Dao et al.*, 1995] show that the temperature inversions bear spatial and temporal characteristics of diurnal tide in the mesosphere. However, the modulation due to semidiurnal tide or other planetary-scale waves can also be important in regions where their amplitudes are large. The modulating mechanisms should be similar to those discussed herein. Recent lidar observations by *Sica et al.* [*personal communication*] have demonstrated clear semidiurnal modulation of the mesospheric temperature inversions.

There are some uncertainties and limitations in the numerical model that should be pointed out. As discussed by *Liu et al.* [1999], the turbulence model is validated for the study of planetary boundary layers, while further validation of the model for mesospheric studies demands more comparisons with accurate measurements. Because the temperature and chemical species changes are critically dependent on the turbulent Prandtl number, it is important to obtain accurate measurement of this quantity. In fact, high-resolution lidar measurements of temperature changes may help determine the turbulence Prandtl number and improve the understanding of the turbulence processes in the mesosphere and mesopause region and thus improve the parameterization of turbulence in this region. Another factor that is not considered in the current study is the radiative processes. Because the radiative cooling rates are 1–2 Kd^{-1} on average, they are assumed to play a less significant role in the development of temperature inversions which occur on timescales of a couple of hours at mesospheric altitudes.

Acknowledgments. We are grateful to John W. Meriwether and Chester S. Gardner for organizing this AGU special session. We wish to thank Christian K. Meyer for valuable comments. We also thank three anonymous reviewers for their helpful comments which motivated the discussion of gravity wave source sensitivity study. The authors acknowledge the support from NASA grants S-97293-E to NCAR. M. E. Hagan also acknowledges the NSF CEDAR program. The National Center for Atmospheric Research is sponsored by the National Science Foundation.

References

Banks, P. M., and G. Kockarts, *Aeronomy, Part B,* 355 pp., Academic, San Diego, Calif., 1973.

Dao, P. D., R. Farley, X. Tao, and C. S. Gardner, Lidar observations of the temperature profile between 25 and 103 km: Evidence of strong tidal perturbation, *Geophys. Res. Lett., 22,* 2825-2828, 1995.

Fritts, D.C., Gravity wave saturation in the middle atmosphere: A review of theory and observations, *Rev. Geophys., 82,* 275-308, 1984.

Fritts, D.C., J. R. Isler, and O. Andreassen, Gravity wave breaking in two and three dimensions, II: Three-dimensional evolution and instability structure, *J. Geophys. Res., 99,* 8109-8123, 1994.

Gardner, C. S., and W. Yang, Measurement of the dynamical cooling rate associated with the vertical transport of heat by dissipating gravity waves in the mesopause region at the Starfire Optical Range, New Mexico, *J. Geophys. Res., 103,* 16,909-16,926, 1998.

Groves, G. V., A global reference atmosphere from 18 to 80 km, *AFGL Tech. Rep., TR-85-0129,* Air Force Geophys. Lab., Bedford, Mass., 1985.

Groves, G. V., Final scientific report, *AFOSR Rep. 84-0045,* Air Force Off. of Sci. Res., Bolling Air Force Base, Washington, D. C., 1987.

Hagan, M. E., J. M. Forbes, and F. Vial, A numerical investigation of the propagation of the quasi 2-day wave into the lower thermosphere, *J. Geophys. Res., 98,* 23,193-23,205, 1993.

Hagan, M. E., J. M. Forbes, and F. Vial, On modeling migrating solar tides, *Geophys. Res. Lett., 22,* 893-896, 1995.

Hagan, M. E., M. D. Burrage, J. M. Forbes, J. Hackney, W. J. Randel, and X. Zhang, GSWM-98: Results for migrating solar tides, *J. Geophys. Res., 104,* 6813-6828, 1999.

Hauchecorne, A., M. L. Chanin, and R. Wilson, Mesospheric temperature inversion and gravity wave breaking, *Geophys. Res. Lett., 14,* 933-936, 1987.

Hedin, A. E., Extension of the MSIS thermosphere model into the middle and lower atmosphere, *J. Geophys. Res., 96,* 1159-1172, 1991.

Holton, J. R., and M. J. Alexander, Gravity waves in the mesosphere generated by tropospheric convection, *Tellus, Ser. A-B, 51,* 45-58, 1999.

Leblanc, T., I. S. McDermid, and D. A. Ortland, Lidar observations of the middle atmospheric thermal tides and comparison with the high-resolution Doppler imager and global-scale wave model, 1, Methodology and winter observations at Table Mountain (34.4°N), *J. Geophys. Res., 104,* 11,917-11,929, 1999a.

Leblanc, T., I. S. McDermid, and D. A. Ortland, Lidar observations of the middle atmospheric thermal tides and comparison with the high-resolution Doppler imager and global-scale wave model, 2, October observations at Mauna Loa (19.5°N), *J. Geophys. Res., 104,* 11,931-11,938, 1999b.

Liu, H.-L., and M. E. Hagan, Local heating/cooling of the mesosphere due to gravity wave and tidal coupling, *Geophys. Res. Lett., 25,* 2941-2944, 1998.

Liu, H.-L., P. B. Hays, and R. G. Roble, A numerical study of gravity wave breaking and impacts on turbulence and mean state, *J. Atmos. Sci., 56,* 2152-2177, 1999.

Mellor, G. L., and T. Yamada, Development of a turbulence closure model for geophysical fluid problems, *Rev. Geophys., 20,* 851-875, 1982.

Meriwether, J. W., X. Gao, K. Beissner, S. Collins, V.B. Wickwar, T.Wilkerson, and M.E. Hagan, Observed coupling of the mesosphere inversion layer to the thermal tidal structure, *Geophys. Res. Lett., 25,* 1479-1482, 1998.

Prusa, J. M., P. K. Smolarkiewicz, and R. R. Garcia, Prop-

agation and breaking at high altitudes of gravity waves excited by tropospheric forcing, *J. Atmos. Sci., 53,* 2186-2216, 1996.

Schmidlin, F. J., Temperature inversions near 75 km, *Geophys. Res. Lett., 3,* 173-176, 1976.

Swenson, G. R., M. J. Taylor, P. J. Espy, C. Gardner, and X. Tao, ALOHA-93 measurements of intrinsic AGW characteristics using airborne airglow and ground-based Na wind/temperature lidar, *Geophys. Res. Lett., 22,* 2841-2844, 1995.

Tao, X., and C. S. Gardner, Heat flux observations in the mesopause region above Haleakala, *Geophys. Res. Lett., 22,* 2829-2832, 1995.

Walterscheid, R. L., Inertio-gravity wave induced accelerations of mean flow having an imposed periodic component: Implications for tidal observations in the meteor region, *J. Geophys. Res., 86,* 9698-9706, 1981.

Walterscheid, R. L., and G. Schubert, Gravity wave fluxes of O_3 and OH at the nightside mesopause, *Geophys. Res. Lett., 16,* 719-722, 1989.

Walterscheid, R. L., and G. Schubert, Nonlinear evolution of an upward propagating gravity wave: Overturning, convection, transience and turbulence, *J. Atmos. Sci., 47,* 101-125, 1990.

Whiteway, J. A., A. I. Carswell, and W. E. Ward, Mesospheric temperature inversions with overlying nearly adiabatic lapse rate: An indication of a well-mixed turbulent layer, *Geophys. Res. Lett., 22,* 1201-1204, 1995.

Yamada, T., Simulations of nocturnal drainage flows by a q^2l turbulence closure model, *J. Atmos. Sci., 40,* 91-106, 1983.

M. E. Hagan, H.-L. Liu, and R. G. Roble, High Altitude Observatory, National Center for Atmospheric Research, P.O.Box 3000, Boulder, CO 80307-3000. (hagan@ucar.edu; liuh@ucar.edu; roble@ucar.edu)

(Received June 5, 1999; revised October 26, 1999; accepted November 18, 1999.)